When classical trajectories get to quantum accuracy: II. The scattering of rotationally excited H 2 on Pd(111)

Alberto Rodríguez-Fernández, Laurent Bonnet, Cedric Crespos, Pascal Larrégaray, Ricardo Díez Muiño

PCCP

ARTICLE TYPE

Cite this: DOI: 00.0000/xxxxxxxxxx

When Classical Trajectories Get to Quantum Accuracy: II. The Scattering of Rotationally Excited H_2 on Pd(111)

Alberto Rodríguez-Fernández,[a,b] Laurent Bonnet,[a,c] Cedric Crespos,[a,c] Pascal Larrégaray,[a,c] and Ricardo Díez Muiño[b,d]

Received Date
Accepted Date

DOI: 00.0000/xxxxxxxxxx

The classical trajectory method in a quantum spirit assigns statistical weights to classical paths on the basis of two semiclassical corrections: Gaussian binning and the adiabaticity correction. This approach was recently applied to the heterogeneous gas-surface reaction between H_2 in its internal ground state and Pd(111) surface *e.g.* [A. Rodríguez-Fernández *et al., J. Phys. Chem. Lett.*, 2019, 10, 7629]. Its predictions of the sticking and state-resolved reflection probabilities were found to be in surprisingly good agreement with those of exact quantum time-dependent calculations where standard quasi-classical trajectory calculations failed. We show in this work that the quality of the previous calculations is maintained or even improved when H_2 is rotationally excited.

Introduction

Constant progress of molecular beam experiments allow to measure with an ever increasing accuracy state-resolved integral and differential cross sections for gas-phase reactions, and sticking or state-resolved reflection probabilities for gas-surface reactions.[1,2] Similar progress are thus required as far as theoretical predictions of these measurements are concerned.

For systems of low dimensionality (typically lower than ~ 6), exact quantum scattering calculations generally provide predictions in excellent agreement with experimental measurements.[3,4] Nowadays, however, more and more reactions of larger dimensionality are under scrutiny.[5–24] For such processes, the quasi-classical trajectory (QCT) method is the only general tool applicable in practice. Besides, the QCT method has a strong interpretative power.[25–27] Nevertheless, quantum corrections must be introduced in these calculations in order to make them realistic when major quantum effects strongly influence the dynamics.

Since the early 2000s, two corrections have been introduced in the QCT method, namely, Gaussian binning[28–33] (GB) and the Adiabaticity correction (AC).[32,34–36] GB introduces some pseudo-quantization in the QCT method by taking into account Bohr's condition of quantization for the final quantized degrees-of-freedom. If one strictly applies Bohr ideas, only those trajectories starting from the reagents with integer actions and reaching the products with integer actions should be taken into account. These trajectories, however, form a set of zero measure compared to the whole set of possible classical paths. To go round this difficulty, trajectories are assigned Gaussian statistical weights such that the closer the final actions to integer values, the larger the weight. For more than 2 or 3 quantized degrees-of-freedom (DOFs) of the final fragments, however, GB lacks precision when applied as such to a quantum state having an energy close to the total energy available.[37] In such a case, a more accurate variant of GB consists in Gaussian weighting the energy deposited on the final quantized DOFs, rather than the actions.[33] Since only one Gaussian weight is involved in this procedure, it is usually called 1GB.[38] We shall use both 1GB and GB in the following. The second correction, AC, takes into account the fact that the QCT method tends to overestimate the statistical weight of those nonreactive trajectories along which the internal motion of the reagents is weakly perturbed and evolves adiabatically. Such trajectories seem to be quite common in complex-forming processes with no entrance barrier. This correction is supported by the semiclassical initial value representation (SCIVR) of molecular collisions.[35,36]

In a recent work,[37] called Part I in the following, the 1GB-AC-QCT approach was applied to the gas-surface reaction H_2 + Pd(111), with H_2 in its rovibrational ground state, and nearly quantitative agreement was found with exact time-dependent quantum scattering calculations. The goal of the present work, called Part II further on, is to check whether this agreement is maintained when H_2 is rotationally excited. We have chosen this specific process because dissociative adsorption, inelastic scattering as well as surface diffraction have been intensively scrutinized both theoretically and experimentally over the last two decades.[39–44] Note that this process takes place on a single elec-

[a] *Université de Bordeaux, ISM, UMR 5255, F-33400 Talence, France.*
[b] *Centro de Física de Materiales CFM/MPC(CSIC-UPV/EHU), Paseo Manuel de Lardizabal 5,20018 Donostia-SanSebastián,Spain.*
[c] *CNRS, ISM, UMR5255, F-33400 Talence, France.*
[d] *Donostia International Physics Center (DIPC), Paseo Manuel de Lardizabal 4,20018 Donostia-SanSebastián,Spain.*

tronic state and involves negligible tunneling. Therefore, no other quantum corrrection than 1GB and AC was found to be necessary.

The paper is laid out as follows. Section 2 details our methodology, which is slightly modified on the basis of SCIVR with respect to Part I in order to improve its consistency with first principles. Briefly, the modification consists in assigning new Gaussian weights to part of the reflected paths implicated in the adiabaticity correction. Our QCT calculations in a quantum spirit, obtained using the methods of both Part I and Part II, are compared with time-dependent quantum scattering calculations in Section 3. Section 4 concludes.

Dynamical Method

We assume that H_2 in the internal state $(v_i = 0, j_i)$ impinges the surface at normal incidence with the collision energy E_i. Eventually, the molecule either sticks on the palladium surface, or bounces back to the vacuum. Whatever the initial rotational excitation, E_i is small enough to make vibrational excitation unavailable after reflection. Our primary goal is to simulate the dynamics of the previous process in the case of the excited rotational states $j_i = 1-4$, though we will also revisit the case $j_i = 0$.

We briefly summarize here the approach described in detail in Part I.[37] For nonreactive trajectories, the four final actions of the system are the vibrational action x_f, the rotational action J_f and the diffractional actions (a_f^n, a_f^m). These are given by:

$$x_f = \frac{1}{2\pi}\oint p dr - \frac{1}{2}, \tag{1}$$

$$J_f = \frac{-1+\sqrt{1+4L_f^2}}{2}, \tag{2}$$

$$a_f^n = \frac{\Delta}{2\pi}P_X^f \tag{3}$$

and

$$a_f^m = \frac{\Delta}{4\pi}\left(P_X^f + \sqrt{3}P_Y^f\right). \tag{4}$$

r is the H_2 bond length and p its conjugate momentum. The cyclic integral in Eq. (1) is calculated by running each trajectory over one vibrational period once H_2 has reached the vacuum, i.e., no longer interacts with the surface. L_f is the modulus of the final classical rotational angular momentum $\boldsymbol{L}_f$ of H_2. Eq. (2) is deduced by equating L_f^2 and $J_f(J_f+1)$. P_X^f and P_Y^f are the projections of the final linear momentum vector of H_2 on the X and Y axis of the Pd(111) surface, chosen in such a way that $(X = 0, Y = 0)$ and $(X = \Delta = 2.75$ Å$, Y = 0)$ are the positions of two nearest neighbour surface atoms. The Z axis is normal to the surface. a_f^n and a_f^m are the classical analogs of Miller indices n and m. Actions are in $\hbar$ unit. We call $\mathbf{a}$ and $\bar{\mathbf{a}}$ the quadruplets (x_f, J_f, a_f^n, a_f^m) and $(\bar{x}_f, \bar{J}_f, \bar{a}_f^n, \bar{a}_f^m)$, respectively, where $\bar{u}$ is the nearest integer of u. Finally, x_i and J_i are the analogs of x_f and J_f for the initial H_2 molecule. x_i and J_i are taken at $v_i = 0$ and j_i, respectively.

In the 1GB approach,[33,38] the statistical contribution to final quantum state $\mathbf{q} = (v_f, j_f, n_f, m_f)$ of a non reactive trajectory ending with $\mathbf{a}$ is given by:

$$w_{1GB}(\mathbf{a},\mathbf{q}) = \frac{1}{\sqrt{\pi\varepsilon}} e^{-\left[\frac{E(\mathbf{a})-E(\bar{\mathbf{a}})}{2\varepsilon E(\mathbf{0})}\right]^2} w_{SB}(\mathbf{a},\mathbf{q}). \tag{5}$$

The right-most term is the statistical weight assigned within the standard binning (SB) procedure. Here, it reads

$$w_{SB}(\mathbf{a},\mathbf{q}) = 2(1+\delta_{\bar{J}_f 0})\delta_{\bar{\mathbf{a}}\mathbf{q}} \tag{6}$$

if $\bar{J}_f$ has the same parity as j_i, 0 in the contrary case. The Kronecker $\delta_{\bar{\mathbf{a}}\mathbf{q}}$ is the usual SB weight corresponding to the boxing procedure. The factor 2 doubles the contribution of trajectories complying with parity conservation, thus, counterbalancing the fact that the remaining trajectories are ignored. The Kronecker delta $\delta_{\bar{J}_f 0}$ takes into account the fact that for $\bar{J}_f = 0$, J_f belongs to the range [0, 0.5] whereas for $\bar{J}_f$ larger than 0, J_f belongs to the range [$\bar{J}_f$ - 0.5, $\bar{J}_f$ + 0.5]. $E(\mathbf{a})$ is the final energy in all the degrees-of-freedom minus the Z-axis orthogonal to the surface. $E(\bar{\mathbf{a}})$ is the analogous energy for quantum state $\bar{\mathbf{a}}$. The mathematical expressions of these energies are given in the section *Energies* of Part I (see Eqs. (5-10)).[37] $E(\mathbf{0})$ is the harmonic zero-point vibrational energy. $w_{1GB}(\mathbf{a},\mathbf{q})$ clearly puts strong emphasis on those trajectories leading to $E(\mathbf{a})$ close to $E(\mathbf{q})$. ε is selected in such a way that $w_{1GB}(\mathbf{a},\mathbf{q})$ takes a significant value for at least $\sim 10^2$ trajectories. In practice, adiabatic non reactive paths are defined by those reflected trajectories involving a single rebound, spending less than 100 fs at a distance from the surface less than 3 Å and leading to the final vibrational action x_f within the narrow range [-0.02, 0.02]. In Part I, these paths were ignored in the statistics. Finally, reactive trajectories are assigned unit statistical weight (sticking is supposed to occur whenever r reaches 2.25 Å and p is positive).

Calling N the total number of trajectories run, excluding adiabatic reflected paths, and N_S the number of trajectories leading to sticking, the sticking probability P_S^I and the probability $P_R^I(\mathbf{q})$ of reflection in quantum state $\mathbf{q}$ used in Part I read:

$$P_S^I = \frac{N_S}{N_S + \Sigma_R^{1GB}} \tag{7}$$

with

$$\Sigma_R^{1GB} = \sum_{\mathbf{q}} \Sigma_R^{1GB}(\mathbf{q}) \tag{8}$$

and

$$\Sigma_R^{1GB}(\mathbf{q}) = \sum_{k=1}^{N-N_S} w_{1GB}(\mathbf{a}_k,\mathbf{q}), \tag{9}$$

and

$$P_R^I(\mathbf{q}) = \frac{\Sigma_R^{1GB}(\mathbf{q})}{N_S + \Sigma_R^{1GB}}. \tag{10}$$

In Eq. (9), the sum is over the non adiabatic reflected trajectories.

We now introduce the modification evoked in the introduction. The upper panel of Fig. 1 shows the rotational state distribution of reflected H_2 molecules for initial j_i equal 0 and an initial collision energy E_i of 65 meV. Two contributions are displayed, corresponding to adiabatic trajectories (blue area) and nonadiabatic trajectories (brown area). Since the discrimination between both

sets of paths used in Part I involves the vibrational action but not the rotational one (see the practical definition of adiabatic paths a bit before Eq. (7)), there can be no assurance that the paths which we called adiabatic in Part I are rotationally adiabatic. In other words, our criterion does not allow to distinguish paths being fully adiabatic (FA), i.e. both vibrationally and rotationally, and paths being partially adiabatic (PA), i.e. vibrationally but not rotationally (note that for simplicity's sake, we ignore diffractional actions in our reasoning). However, we have a visual way of detecting the existence of type-FA paths: these imply in the rotational state distribution a single narrow peak centered at j_i (here, 0), such as the one visible in the blue distribution of the upper panel of Fig. 1. We will define it by $\bar{J}_f = 0$ further on. Such peaks are indeed due to compact volumes of initial conditions which all lead to $J_f \sim j_i$. For the process at hand, however, the peak is only visible for $j_i = 0$ and E_i lower than ~90 meV. In the following, we will assume that the peak is entirely due to fully adiabatic paths. In all other cases, no peak has been found, as illustrated in the lower panel of Fig. 1. The rotational state distribution for $j_i = 1$ and the same collision energy as previously is indeed flat around $J_f = 1$. Consequently, the adiabaticity is only partial in this case. For the sake of rigor, we now modify our formulation of the statistical weights in order to take into account the previous observations.

As a first step, it is necessary to examine how type-FA trajectories look like. We have thus randomly selected a few tens of paths among the ones contributing to the narrow peak previously considered. It is found that they all rebound against the Pd(111) surface in the neighborhood of a bridge site. Moreover, the distribution of the polar angle θ with respect to the Z-axis at the instant of the rebound is found from Fig. 2 to be strongly polarized, while the distribution of the azimuth angle ϕ is uniform. The time-dependences of the distance Z between H_2 and the surface on one hand, and the potential energy on the other hand, are displayed in Fig. 3. At time 0, the incoming H_2 is at ~ 7 Å from the Pd surface with a collision energy of 65 meV and a normal incidence. Until ~ 100 fs, Z linearly varies in the course of time, thus implying that H_2 does not interact with the surface. However, the process is barrierless in the entrance channel, so at some point, the H_2 molecule experiences an attractive force which accelerates its motion towards the Pd surface. The slope of the blue curve, thus, becomes slightly stronger from ~ 120 fs up to ~ 200 fs, where the rebound takes place. The rest of the blue curve is nearly symmetric with respect to 200 fs, illustrating thereby the full adiabaticity of the internal motion of H_2; back to the vacuum, nothing has changed, neither its vibrational energy, nor its rotational energy, nor the direction of its velocity vector, still orthogonal to the Pd surface. As for the potential energy (see Fig. 3), its time dependence is consistent with the previous curve. Since the incoming H_2 is vibrating, the potential energy strongly oscillates. The minima, fitted by the red line, correspond to those instants where the bond length of H_2 takes its equilibrium value. They thus define the interaction potential energy between H_2 and the surface. The whole potential is thus given by the sum of this interaction potential and the vibrational potential of H_2. In the region of the configuration space (X,Y,Z,r,θ,ϕ) visited by type-

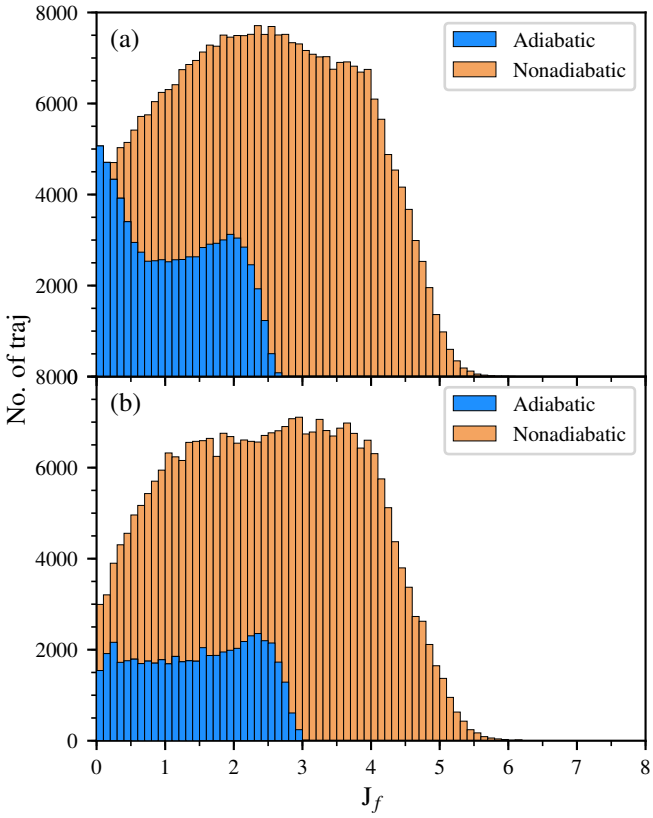

Fig. 1 Rotational state distribution of reflected H_2 molecules for E_i = 65 meV, $j_i = 0$ (panel a) and $j_i = 1$ (panel b). The blue and brown contributions are due to adiabatic and nonadiabatic paths, respectively. In ordinate, the trajectory number is for each bar of the histogram. In panel a, the peak in the blue distribution is due to paths being both vibrationally and rotationally adiabatic (see text for further details).

FA trajectories, the interaction potential is expected to be nearly independent on (X,Y,θ,ϕ). Otherwise, some energy would be transfered to these coordinates during the collision, perturbating thereby the rotational motion of H_2 as well as its motion parallel to the (X,Y) plane, which is not the case. The interaction potential along type-FA paths can thus be approximated by a function of Z alone. Since the time dependence of Z is roughly linear except during the rebound, the Z-dependence of the previous function has nearly the same shape as the fit of the minima (red curve in Fig. 3) deep into the well.

We now modify the method of Part I within a reduced dimensional semiclassical treatment taking into account the key topographical features of the interaction potential discussed above. The dimensional reduction is aimed at simplifying the following mathematical developments while preserving the essence of the dynamics involved in the title process. The treatment is as follows: we freeze the X, Y and ϕ coordinates, being thus left with Z, r and θ. H_2 is thus a vibrator and planar rotator (supposed to rotate within the (X,Z) plane) whose center-of-mass is constrained to lie on the Z-axis. In three dimensions, θ belongs to the range $[0,\pi]$, but here, it belongs to the range $[0,2\pi]$. The phase space state of the system is thus (Z,r,θ,P,p,J), where P is the linear momentum conjugate to Z and J is the rotational ac-

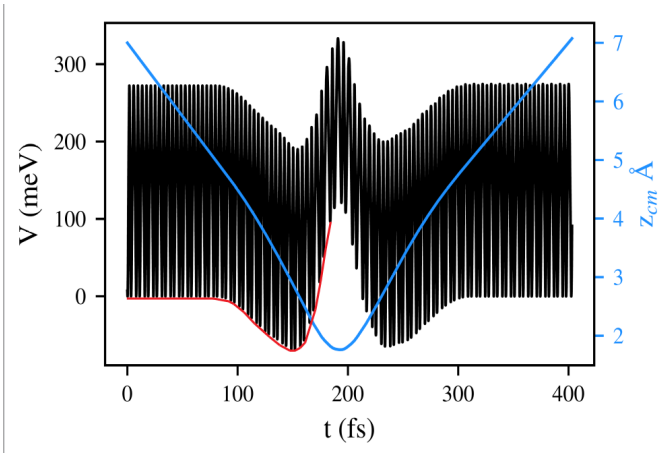

Fig. 2 Distribution of the polar angle θ at the instant of the rebound against the Pd(111) surface for type-FA trajectories.

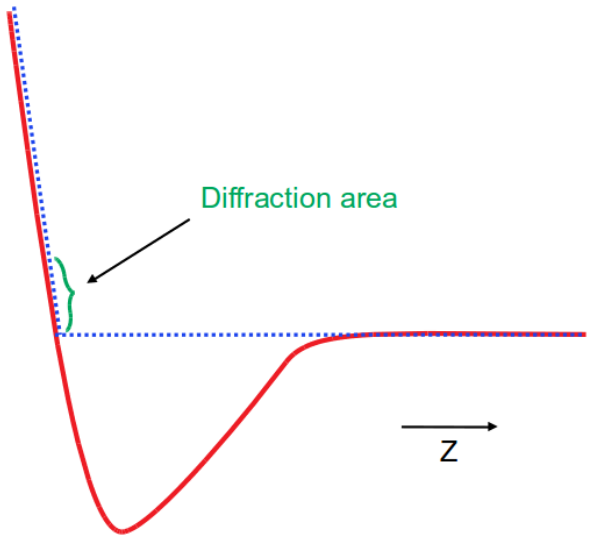

Fig. 3 Time-dependence of the distance Z between the center-of-mass of H_2 and the surface for a typical type-FA trajectory (blue curve); same dependence for the potential energy (black curve).

tion (or angular momentum in $\hbar$ unit) conjugate to θ (p is defined right below Eq. (4)). However, the semiclassical treatment used in the following makes use of action angle coordinates for the internal DOFs, so we will alternately specify the phase space state by (Z,q,θ,P,x,J), where q is the vibrational phase of H_2 and x is the vibrational action conjugate to q. We assume that H_2 is in the initial state $(v_i=0, j_i=0)$. We denote the mass of H_2 by μ, its vibrational frequency by ω and its moment of inertia by I. We call $S_{v_f j_f}$ the probability amplitude that after reflection, H_2 is in the final state (v_f, j_f). Following Miller,[45,46] this scattering matrix element can be expressed in terms of classical paths as:

$$S_{v_f j_f} = \frac{1}{4\pi^2}\int dq_i^s d\theta_i^s \left|\frac{\partial q_f^s}{\partial q_i^s}\frac{\partial \theta_f^s}{\partial \theta_i^s} - \frac{\partial q_f^s}{\partial \theta_i^s}\frac{\partial \theta_f^s}{\partial q_i^s}\right|^{1/2} exp\left(i\left[(x_f - v_f)q_f^s + (J_f - j_f)\theta_f^s + \Omega_{fi}\right]\right) \quad (11)$$

with

$$\Omega_{fi} = -\int_0^t d\tau \left(Z\dot{P} + q\dot{x} + \theta\dot{J}\right). \quad (12)$$

q^s and θ^s are the shifted angles defined by

$$q^s = q - \frac{\mu Z\omega}{P} \quad (13)$$

and

$$\theta^s = \theta - \frac{\mu ZJ}{PI}. \quad (14)$$

Contrary to q and θ, q^s and θ^s have the property to be constant in the asymptotic channel, i.e., they only evolve within the interaction region. Like for quantum numbers, the labels i and f assigned in Eq. (11) to q^s and θ^s refer to their initial and final values, respectively. The trajectories used to calculate $S_{v_f j_f}$ are started at Z_i and stopped at Z_f, distances beyond which H_2 is uncoupled with the surface. Time τ is equal to 0 at Z_i and t at Z_f. The initial conditions are the negative value of P corresponding to the collision energy E_i, $x_i = v_i = 0$, $J_i = j_i = 0$, q_i^s and θ_i^s. q_f^s, θ_f^s, x_f, J_f and Ω_{fi} are functions of q_i^s and θ_i^s. We note that Eq. (14) and the fact that $J_i = 0$ make θ_i^s and θ_i equal. For simplicity's sake, we ignore the phase index necessary for an accurate description of interference effects.[47] Historically, Eq. (11) is the starting point of the SCIVR,[45,46,48,49] remarkably accurate for direct inelastic collisions,[45,47,50] direct collinear reactions[51,52] and molecular spectroscopy.[53,54] The interested reader will find detailed developments on SCIVR in the previously mentioned references and references therein.

In line with our previous observations, we assume that among the trajectories defined above, type-FA trajectories are those for which H_2 is nearly perpendicular to the Pd surface at the instant of the rebound. For simplicity's sake, we also assume that along these paths, there is no stiring effect reorienting H_2 on way to the surface; the approaching H_2 diatom is thus supposed to be already oriented nearly perpendicular to the surface before experiencing the attractive forces. In the following, we define type-FA paths as those for which θ_i^s belongs to the two ranges of width Δ respectively centered at 0 and π (since θ_i^s belongs to the range $[0,2\pi]$, the range of width Δ "centered" at 0 is $[0,\Delta/2]\cup[2\pi-\Delta/2,2\pi]$). The interaction potential met by type FA-paths, assumed to have the shape of the red curve in Fig. 3, is represented in terms of Z in Fig. 4 (also in red). In a preliminary step, however, we will consider the simple model of interaction potential corresponding to the blue dashed curve. This potential involves the same strongly repulsive wall but no well. We emphasize that the interaction potential felt by type-FA trajectories is the same for all of them, i.e., the potential does not depend on θ^s within the two previously defined ranges of width Δ. The rest of the trajectories (type-PA plus type-NA, NA meaning non adiabatic) are defined by angular ranges which are not necessary to specify. Each type of path is assumed to remain of the same type when modifying its initial vibrational phase q_i^s within $[0,2\pi]$. This assumption was validated from trajectory calculations. At last, since our purpose here is to reweight reflected trajectories, we assume that no reactive trajectory leading to sticking is involved in the present process model.

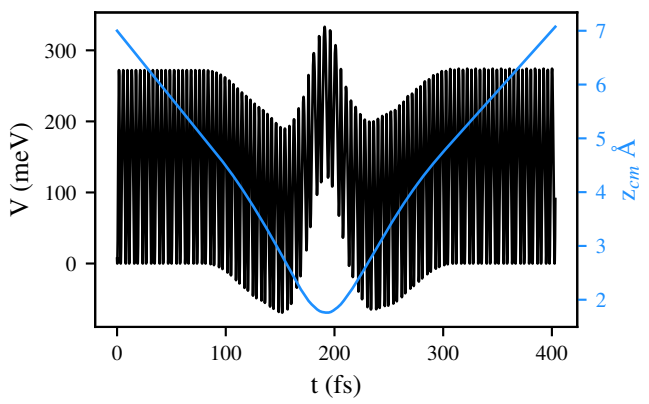

Fig. 4 Realistic Z-dependence of the interaction potential energy for H_2/Pd(111) (red curve); simple model of interaction potential involving the same repulsive wall as the red curve followed by a flat potential up to the vacuum (blue dashed curve).

We now come back to Eq. (11) and focus on the contribution $S^{FA}_{v_f j_f}$ to $S_{v_f j_f}$ due to type-FA paths. As previously stated, we start with the blue dashed interaction potential in Fig. 4. Along type-FA paths, the internal motion of H_2 is conserved, i.e., $\dot{x} = \dot{J} = 0$ (it was numerically checked in a previous study[35] that $\dot{x} = 0$ along both type-FA and type-PA paths). Consequently, $x_f = x_i = 0$ and $J_f = J_i = 0$. Second, the time dependence of Z along type-FA paths is identical for all these paths (they are supposed to bounce off the wall in the same manner since the latter is isotropic within the previously defined ranges of width Δ); from Eq. (12), we thus see that Ω_{fi} takes the same value Ω^{FA}_{fi} for all fully adiabatic paths. Third, one may show that $\frac{\partial q^s_f}{\partial q^s_i} = \frac{\partial \theta^s_f}{\partial \theta^s_i} = 1$ (see Eqs. (17) to (19) in Ref.[47]). Fourth, $\frac{\partial q^s_f}{\partial \theta^s_i} = \frac{\partial \theta^s_f}{\partial q^s_i} = 0$ (the vibrational and rotational motions are uncoupled along type-FA trajectories). Using these relations, one can exactly integrate the right-hand-side (RHS) of Eq. (11) over the initial angles corresponding to type-FA paths (we recall that q^s_i belongs to $[0, 2\pi]$ while θ^s_i belongs to $[0, \Delta/2] \cup [\pi - \Delta/2, \pi + \Delta/2] \cup [2\pi - \Delta/2, 2\pi]$). After some mathematical steps, one finds:

$$S^{FA}_{v_f j_f} = \delta_{0 v_f} \frac{sin(\frac{\Delta j_f}{2})}{\pi j_f} [1 + e^{-i\pi j_f}] e^{i\Omega^{FA}_{fi}} \tag{15}$$

($\delta_{0 v_f}$ is Kronecker delta). One immediately sees that according to SCIVR, type-FA trajectories do not contribute to the vibrational excitation of H_2, in agreement with the classical description. On the other hand, they can contribute to its rotational excitation, against common sense. In the present case, rotational excitation is nothing else than the consequence of a diffraction process (see Fig. (3) in Ref.[35]). One notes that semiclassical theory respects the fact that for homonuclear diatomic molecules, odd transitions are prohibited.

Along type-PA trajectories, the interaction potential is supposed to depend on θ. The rotational motion is thus perturbed throughout the rebound against the strongly repulsive wall. On the other hand, the vibrational motion is nearly uncoupled with the rotational motion so we can neglect its perturbation. Consequently, $\dot{x} = 0$, $x_f = x_i = 0$, $\frac{\partial q^s_f}{\partial q^s_i} = 1$ and $\frac{\partial q^s_f}{\partial \theta^s_i} = 0$. Integrating the RHS of Eq. (11) over q^s_i as before and using the stationary phase approximation[45,47,55,56] to integrate over θ^s_i leads to the contribution to $S_{v_f j_f}$ due to type-PA paths:

$$S^{PA}_{v_f j_f} = \delta_{0 v_f} \frac{1}{\sqrt{2\pi}} \sum_{Paths} \left| \frac{\partial J_f}{\partial \theta^s_i} \right|^{-1/2} e^{i\Omega^{PA}_{fi}} \tag{16}$$

(it is unnecessary to specify Ω^{PA}_{fi} which will disappear in the following). The sum is over those paths complying with the boundary conditions $J_f = j_f$.

For type-NA trajectories, one still uses the stationary phase approximation[45,55,56] to integrate the RHS of Eq. (11) over both angles corresponding to type-NA paths. The final result provides the contribution to $S_{v_f j_f}$ due to these paths:

$$S^{NA}_{v_f j_f} = \frac{1}{2\pi} \sum_{Paths} \left| \frac{\partial x_f}{\partial q^s_i} \frac{\partial J_f}{\partial \theta^s_i} - \frac{\partial x_f}{\partial \theta^s_i} \frac{\partial J_f}{\partial q^s_i} \right|^{-1/2} e^{i\Omega_{fi}}. \tag{17}$$

The sum is over those paths complying with the boundary conditions $x_f = v_f$ and $J_f = j_f$. The rotational term in the RHS of Eq. (16) and the RHS of Eq. (17) are standard expressions of classical S-matrix theory.[45,56]

When (i) squaring the modulous of the full S-matrix element $S^{FA}_{v_f j_f} + S^{PA}_{v_f j_f} + S^{NA}_{v_f j_f}$, (ii) using the results of Refs.[57,58] to make delta distributions appear, and (iii) neglecting interference terms generally quenched in realistic situations by summing over non measurable quantum numbers (see Sec. 2.2 in Ref.[59]), the whole population of state (v_f, j_f) appears to be given by $P^{FA}_{v_f j_f} + P^{PA}_{v_f j_f} + P^{NA}_{v_f j_f}$ with

$$P^{FA}_{v_f j_f} = 2\delta_{0 v_f} [1 + (-1)^{j_f}] \left[\frac{sin(\frac{\Delta j_f}{2})}{\pi j_f} \right]^2, \tag{18}$$

$$P^{PA}_{v_f j_f} = \frac{\delta_{0 v_f}}{2\pi} \int_{PA\ paths} d\theta^s_i\ \delta(J_f - j_f) \tag{19}$$

and

$$P^{NA}_{v_f j_f} = \frac{1}{4\pi^2} \int_{NA\ paths} dq^s_i d\theta^s_i\ \delta(x_f - v_f) \delta(J_f - j_f). \tag{20}$$

We now consider the realistic red interaction potential in Fig. 4. Unlike the previous case, the diffraction created by the rebound against the isotropic repulsive wall may rotationally excite H_2 within the well to such an extent that H_2 has not enough translational energy along the Z coordinate to come back to the vacuum. If so, H_2 is trapped within the well. This is what we previously called diffraction-mediated trapping.[35] If the collision energy E_i is very small, j_f can only be 0. On the other hand, diffraction may excite many rotational states within the well where the available energy is much larger than in the vaccum. Hence, the probability that the $j_f = 0$ state is excited is small. Since this probability is also the probability that H_2 turns back to the vacuum, diffraction-mediated trapping (DMT) is expected to be important. As in previous works, we assume it to be total, i.e., all the diffracted wave is trapped. If so, the latter eventually contributes to both sticking and inelastic bouncing, just as the rest of the incident wave.

The classical transposition of this DMT scenario is that the probability carried by adiabatic paths is redistributed to the remaining paths. For simplicity's sake, we assume that the redistribution is democratic, so one may ignore adiabatic paths and renormalize to unity the probability carried by the remaining trajectories.[35–37] Moreover, Eq. (19) suggests that type-PA paths should be assigned thin Gaussian weights $G(J_f - j_f) = exp[-(J_f - j_f)^2/\varepsilon^2]/(\sqrt{\pi}\varepsilon)$ in order to mimic the delta function (see Eq. (11) in Ref.[29]; ε is generally taken at 0.06, thus making the Gaussian 10% wide). Finally, Eq. (20) suggests that type-NA paths should be assigned the product of Gaussian weights $G(x_f - v_f)G(J_f - j_f)$. Now, if all the dimensions of the process are taken into account, the weights for type-PA paths will depend on the final diffractional actions a_f^n and a_f^m in addition to J_f whereas the weights for type-NA paths will depend on all the final actions, as in our previous calculations (see Part I).[37] For type-PA trajectories, we chose the product $G(J_f - j_f)G(a_f^n - n_f)G(a_f^m - m_f)$ of three Gaussian weights, each one depending on a single action, while for type-NA paths, we chose the same 1GB weights as in Part I,[37] given by Eqs. (5) and (6) of this work. These choices have been made so as to maximize the accuracy of our calculations at the thresholds of new quantum states given the number of trajectory results available.

To recapitulate, the sticking probability obtained when dividing in four sets the whole bunch of trajectories run [(i) reactive, (ii) type-FA, (iii) type-PA and (iv) type-NA)] reads:

$$P_S^{II} = \frac{N_S}{N_S + \Sigma_R^{NA} + \Sigma_R^{PA}} \tag{21}$$

where

$$\Sigma_R^{NA} = \sum_{\mathbf{q}} \Sigma_R^{NA}(\mathbf{q}) \tag{22}$$

with

$$\Sigma_R^{NA}(\mathbf{q}) = \sum_{k=1}^{N_{NA}} w_{1GB}(\mathbf{a}_k, \mathbf{q}), \tag{23}$$

and

$$\Sigma_R^{PA} = \sum_{\mathbf{q}} \Sigma_R^{PA}(\mathbf{q}) \tag{24}$$

with

$$\Sigma_R^{PA}(\mathbf{q}) = \sum_{k=1}^{N_{PA}} w_{GB}(\mathbf{a}_k, \mathbf{q}), \tag{25}$$

$$w_{GB}(\mathbf{a}, \mathbf{q}) = G(J_f - j_f)G(a_f^n - n_f)G(a_f^m - m_f)w_{SB}(\mathbf{a}, \mathbf{q}) \tag{26}$$

and

$$G(u) = exp[-u^2/\varepsilon^2]/(\sqrt{\pi}\varepsilon). \tag{27}$$

As previously, N_S is the number of trajectories leading to sticking and type-FA paths are ignored. Moreover, N_{NA} and N_{PA} are the numbers of type-NA and type-PA trajectories. In Eqs. (23) and (25), the sums are obviously over the type-NA and type-PA trajectories, respectively. Finally, the state-resolved reflection probability reads:

$$P_R^{II}(\mathbf{q}) = \frac{\Sigma_R^{NA}(\mathbf{q}) + \Sigma_R^{PA}(\mathbf{q})}{N_S + \Sigma_R^{NA} + \Sigma_R^{PA}}. \tag{28}$$

The type of calculations published in Part I (or using Eqs. (7)–(10) in the present work) will be called QCT-SC-I whereas those reported in the present Part II, based on Eqs. (21)–(28), will be called QCT-SC-II (SC stands for "semiclassically corrected"). It is worth reiterating that in QCT-SC-I calculations, trajectories are either (i) reactive, or (ii) type-NA reflected, or (iii) type-A reflected–A being for adiabatic–regardless of whether they are type-FA or type-PA. Three sets of paths are thus dealt with in QCT-SC-I calculations, against four in QCT-SC-II ones.

Results and discussion

The classical trajectory calculations were performed by means of the Density-Functional-Theory-based ground state potential energy surface of Busnengo *et al.*[60,61] The Bulirsch-Stoer integrator was used with an initial time step of 0.01 fs. Trajectories were started at $Z = 5$ Å with normal incidence. Reflected paths were stopped at the same value of Z and reactive trajectories at $r = 2.5$ Å. For H_2 in the initial state $(v_i = 0, j_i = 1)$, a total of 133 energies spaced 3 meV aparts were considered within the range 2 – 398 meV, and 800 000 trajectories were run at each energy. For the rest of the initial states, 50 energies were considered within the range 2 – 149 meV with the same energy spacing and number of trajectories per energy as previously. A few calculations beyond 149 meV showed that the differences between quantum and classical results are no longer significant.[62] In any cases, the Gaussian width parameter ε was taken at 0.003 and 0.06 for the calculation of 1GB and GB weights, respectively.

Fig. 5 shows the quantum time-dependent wave-packet (Q-TDWP)[40,62] and purely classical (QCT) sticking probabilities for H_2 in the initial state $(v_i = 0, j_i = 1)$. Clearly the QCT method fails to correctly reproduce the uneven structure of the quantum probability below ~270 meV. This behavior is similar to that observed when H_2 is in the initial state $(0,0)$.[63] On the other hand,

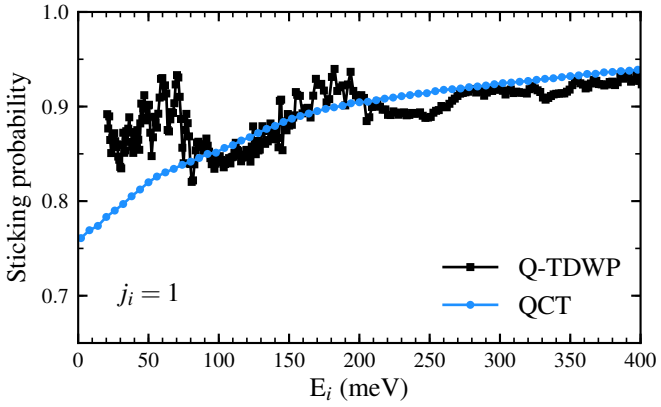

Fig. 5 Quantum (black squares) and standard QCT (blue circles) sticking probabilities for $H_2(0,1)$ + Pd(111) as a function of the collision energy.

it is shown in panel (a) of Fig. 6 that the QCT-SC-I and QCT-SC-II approaches clearly reproduce the quantum structures. Two vertical dashed-dotted lines are drawn at the energies corresponding to the opening of the rotational excitation channels $1 \rightarrow 3,5$ where a drop of the sticking probability is observed. The remaining panels of Fig. 6 show the collision energy dependence of the rotationally elastic and inelastic reflection probabilities. Panels (b), (c) and (d) correspond to final rotational states $j_f = 1$, 3 and 5, respectively. The vertical dashed-dotted lines in panels (c)

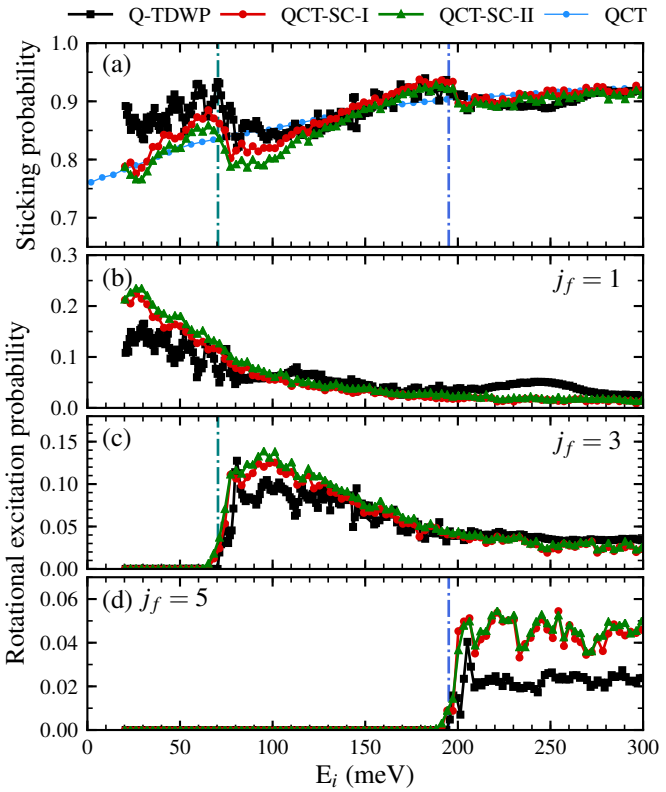

Fig. 6 Panel (a): collision energy dependence of the sticking probability for $H_2(0,1)$ + Pd(111) according to quantum (black squares), QCT-SC-I (red circles) and QCT-SC-II (green triangles) calculations. The standard QCT sticking probability is also plotted for comparison purposes (blue circles). Panels (b-d): same as before for the rovibrationally elastic and inelastic scattering probabilities. The final rotational states $j_f = 1$, 3 and 5 are specified in each panel (the final vibrational quantum number is necessarily zero).

and (d) correspond to those of panel (a) and the QCT-SC-I and QCT-SC-II curves accurately describe the thresholds corresponding to the opening of the (0,3) and (0,5) states, in agreement with the quantum probabilities. We note that below ~120 meV, the QCT-SC-II sticking probability (green curve in panel (a)) is slightly lower than the QCT-SC-I probability (red curve). This is due to the fact that type-PA reflected trajectories are not ignored in QCT-SC-II calculations while they are in QCT-SC-I calculations. Since in the present case, the disagreement with quantum mechanics is increased by the account of type-PA trajectories, these are likely to be more rotationally adiabatic and, thus, more fully adiabatic than expected from our criterion to distinguish between type-FA and type-PA trajectories. This suggests that this criterion should be refined. We note that the larger the collision energy, the stronger the couplings between translational, vibrational and rotational motions within the interaction region, the smaller the amount of adiabatic trajectories and the closer the green and red curves (whenever there are no adiabatic paths, QCT-SC-I (Eqs. (7)-(10)) and QCT-SC-II (Eqs. (21)-(28)) methods lead to strictly the same predictions).

For higher initial rotational excitations ($j_i = 2-4$), sticking probabilities are displayed in Fig. 7 while rotationally elastic and inelastic reflection probabilities are represented in Fig. 8. The agreement between the QCT predictions in a quantum spirit and the quantum results appears to be even better than for $j_i = 0$ (see Part I[37] and below) and $j_i = 1$. On the other hand, standard QCT calculations make disappear any structure in the probabilities, as for $j_i = 0$ and 1. The drops in the sticking probabilities at 98 meV for $j_i = 2$, and 125 meV for $j_i = 3$ (see panels (a) and (b) of Fig. 7), correspond to the openings of the rotational excitation channels $2 \rightarrow 4$ and $3 \rightarrow 5$, as clearly seen in panels (a) and (b) of Fig. 8. In both cases the thresholds are very well described.

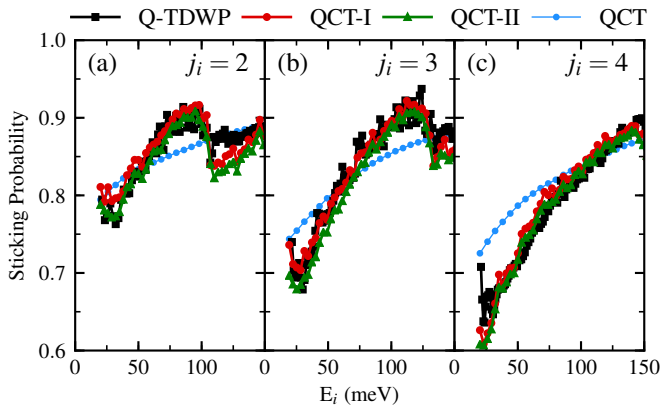

Fig. 7 Collision energy dependence of the sticking probabilities for $H_2(0, j_i = 2-4)$ + Pd(111) according to quantum (black squares), QCT-SC-I (red circles), QCT-SC-II (green triangles) and standard QCT (blue circles) calculations.

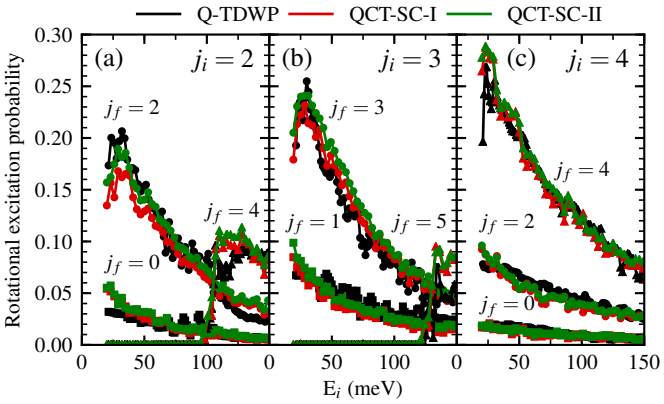

Fig. 8 Collision energy dependence of rovibrationally elastic and inelastic scattering probabilities for $H_2(0,\ j_i = 2-4)$ + Pd(111) according to quantum (black symbols), QCT-SC-I (red symbols) and QCT-SC-II (green symbols) calculations. Final rotational states are indicated close to their corresponding curves.

Finally, we applied our new QCT-SC-II approach to the case $(v_i = 0, j_i = 0)$, using the same energy spacing and trajectory amount per energy as in Part I. We recall that among adiabatic paths, type-FA paths were identified as those leading to $\bar{J}_f = 0$ for E_i lower than ~90 meV (see the discussion around Fig. 1). The resulting sticking probability is represented by the green triangles in Fig. 9. The red circles in the same figure were obtained by means

of the QCT-SC-I approach. Above $\sim$ 40 meV, the green sticking probability is slightly lower than the red one, as for $j_i = 1$, since the former takes into account more reflected trajectories than the latter. We note that above $\sim$ 200 meV, QCT-SC-II probabilities are in slightly better agreement with QM probabilities than QCT-SC-I ones. On the other hand, it is quite probable that below 40 meV, most adiabatic paths are type-FA paths. In such case, the two formulations lead to the same predictions (compare Eqs. (7)-(10) with Eqs. (21)-(28)), and the red and green curves overlap, as observed in Fig. 9.

Although in the case of the H_2/Pd(111) system, the QCT-SC-II method leads to predictions very similar to the QCT-SC-I method, the former is based on a more rigorous application of semiclassical scattering theory than the latter. Moreover, the calculations are of the same difficulty (or simplicity) for both approaches. We might thus be more inclined to use the QCT-SC-II method in future studies.

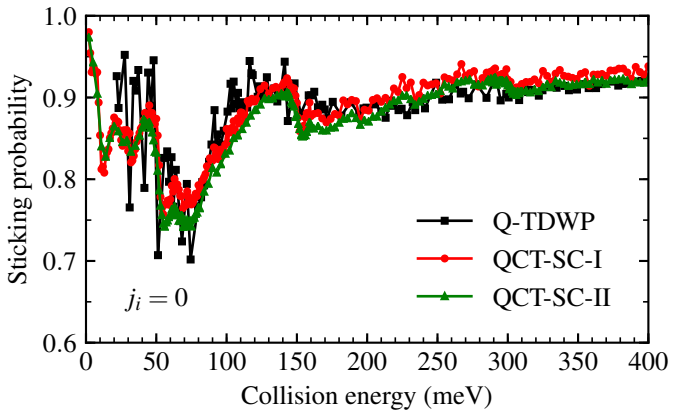

Fig. 9 Collision energy dependence of the sticking probability for H_2(0, 0) + Pd(111) according to quantum (black symbols), QCT-SC-I (red symbols) and QCT-SC-II (green symbols) calculations.

Conclusions

The classical approach in a quantum spirit, initially devised for gas-phase reactions, differs from the standard quasiclassical trajectory (QCT) method by the statistical weights finally assigned to the trajectories. While these weights are identical for all the trajectories in the QCT method, they are either Gaussian,[28,29,32,33,38] or simply zero[32,34–36] for the previous approach. Gaussian weights take into account Bohr's condition of quantization for the final bounded degrees-of-freedom. Zero weights take into account the fact that, within the quantum picture, some parts of the incident wave may be diffracted at very small collision energies. The first type of weighting is called Gaussian binning (GB[28,29,32] or 1GB[33,38]) while the second is called adiabaticity correction (AC).[32,34–36]

In a recent work (Part I),[37] we applied the 1GB-AC-QCT method to the heterogeneous gas-surface reaction between H_2 in its internal ground state and Pd(111) surface. The sticking probability and the state-resolved reflection probabilities obtained by means of this approach were found to be in close agreement with the corresponding probabilities obtained from exact quantum scattering calculations. In contrast, the standard QCT method fails to reproduce the previous quantities, except in the high energy limit (as it should be).

The purpose of this work was to check whether the previous agreement was maintained when H_2 is rotationally excited. We not only applied the method of Part I, but also a variation of it regarding the adiabaticity correction, put on firmer semiclassical grounds than the method of Part I. The results displayed in Figs. 6–9, of similar quality for both methods, provide a very positive answer. The rugged collision energy dependences of quantum sticking probabilities are accurately reproduced for all the rotational excitations considered. This comment holds for the state-resolved reflection probabilities, particularly around the opening of inelastic channels. As a matter of fact, for non activated reactions at relatively low energies, our two-part study shows that the classical approach in a quantum spirit offers a remarkable description of gas-surface reaction dynamics features that the QCT method in its standard implementation is unable to provide.

Conflicts of interest

There are no conflicts to declare.

Acknowledgements

A.R.F. acknowledges financial support by the Université de Bordeaux. The authors acknowledge the support of France Grilles for providing computing resources on the French National Grid Infrastructure. Computer time was provided as well by the Pôle Modélisation HPC facilities of the Institut des Sciences Moléculaires, UMR 5255, CNRS, Université de Bordeaux, co-funded by the Nouvelle Aquitaine region as well as the MCIA (Mésocentre de Calcul Intensif Aquitain) ressources of the Université de Bordeaux and of the Université de Pau et des Pays de l'Adour. This work was conducted in the scope of the transborder joint Laboratory "QuantumChemPhys: Theoretical Chemistry and Physics at the Quantum Scale (ANR-10-IDEX-03-02)." RDM acknowledges financial support by the Gobierno Vasco-UPV/EHU Grant No. IT-1246-19. Finally, we wish to thank Dr. Cristina Diaz, of the Universidad Autónoma de Madrid, for providing us with the Q-TDWP results.

Notes and references

1 H. Pan, K. Liu, A. Caracciolo and P. Casavecchia, *Chem. Soc. Rev.*, 2017, **46**, 7517–7547.
2 X. Yang, D. C. Clary and M. Neumark, *Chem. Soc. Rev.*, 2017, **46**, 7481.
3 D. H. Zhang and H. Guo, *Annu. Rev. Phys. Chem.*, 2016, **67**, 135.
4 B. Fu, X. Shan, D. H. Zhang and D. C. Clary, *Chem. Soc. Rev.*, 2017, **46**, 7625.
5 H. Chadwick and R. D. Beck, *Chem. Soc. Rev.*, 2016, **45**, 3576.
6 H. Pan, K. Liu, A. Caracciolo and P. Casavecchia, *Chem. Soc. Rev.*, 2017, **46**, 7517.
7 A. J. Orr-Ewing, *Chem. Soc. Rev.*, 2017, **46**, 7597.
8 F. Nattino, D. Migliorini, G.-J. Kroes, E. Dombrowski, E. A.

High, D. R. Killelea and A. L. Utz, *J. Phys. Chem. Lett.*, 2016, **7**, 2402.
9 M. Braunstein and P. Conforti, *J. Phys. Chem. A*, 2015, **119**, 3311–3322.
10 G. Czakó, Y. Wang and J. Bowman, *J. Chem. Phys.*, 2011, **135**, 151102.
11 A. Matsugi, *J. Phys. Chem. A*, 2015, **119**, 1846–1856.
12 L. Ping, L. Tian, H. Song and M. Yang, *J. Phys. Chem. A*, 2018, **122**, 6997–7005.
13 S. A. Vázquez, X. L. Otero and E. Martinez-Nunez, *Molecules*, 2018, **23**, 3156.
14 J. Espinosa-Garcia and J. C. Corchado, *Theor. Chem. Acc.*, 2015, **134:6**, year.
15 J. Espinosa-Garcia, *J. Phys. Chem. A.*, 2016, **120**, 5–13.
16 J. Espinosa-Garcia and J. C. Corchado, *J. Phys. Chem. B.*, 2016, **120**, 1446–1453.
17 K. Shao, B. Fu and D. H. Zhang, *Phys. Chem. Chem. Phys.*, 2015, **17**, 24098–24107.
18 L. Bonnet, R. Linguerri, M. Hochlaf, O. Yazidi, P. Halvick and J. S. Francisco, *J. Phys. Chem. Lett.*, 2017, **8**, 2420–2424.
19 V. Macaluso, Z. Homayoon, R. Spezia and W. L. Hase, *Phys. Chem. Chem. Phys.*, 2018, **20**, 19744–19749.
20 J. Loreau, A. Faure and F. Lique, *J. Chem. Phys.*, 2018, **148**, 244308.
21 O. Roncero, A. Zanchet and A. Aguado, *Phys. Chem. Chem. Phys.*, 2018, **20**, 25951–25958.
22 T. Nagy and G. Lendvay, *J. Phys. Chem. Lett.*, 2017, **8**, 4621–4626.
23 S. Góger, P. Szabó, G. Czakó and G. Lendvay, *Energy Fuels*, 2018, **32**, 10100–10105.
24 T. Kasai, D. Che, P. Tsai, M. Nakamura, B. Muthiah and K.-C. Lin, *Rendiconti Lincei, Scienze Fisiche e Naturali*, 2018, **29**, 219–232.
25 J. Polanyi, *Acc. Chem. Res.*, 1972, **5**, 161–168.
26 F. Bouakline, S. C. Althorpe, P. Larregaray and L. Bonnet, *Mol. Phys.*, 2010, **108**, 969–980.
27 H. Guo and B. Jiang, *Acc. Chem. Res.*, 2014, **47**, 3679–3685.
28 L. Bonnet and J. Rayez, *Chem. Phys. Lett.*, 1997, **277**, 183.
29 L. Bonnet and J.-C. Rayez, *Chem. Phys. Lett.*, 2004, **397**, 106.
30 M. L. González-Martínez, W. Arbelo-González, J. Rubayo-Soneira, L. Bonnet and J.-C. Rayez, *Chem. Phys. Lett.*, 2008, **463**, 65–71.
31 J. D. Sierra, L. Bonnet and M. González, *J. Phys. Chem. A*, 2011, **115**, 7413âĂŞ7417.
32 L. Bonnet, *Int. Rev. Phys. Chem.*, 2013, **32**, 171.
33 G. Czakó and J. M. Bowman, *J.Chem. Phys.*, 2009, **131**, 244302.
34 L. Bonnet, *J. Chem. Phys.*, 2008, **128**, 044109.
35 C. Crespos, J. Decock, P. Larrégaray and L. Bonnet, *J. Phys. Chem. C*, 2017, **121**, 16854.
36 L. Bonnet, P. Larregaray, M. Lara and J.-M. Launay, *J. Phys. Chem. A*, 2019, **123**, 6439–6454.
37 A. Rodríguez-Fernández, L. Bonnet, C. Crespos, P. Larrégaray and R. Díez Muiño, *The Journal of Physical Chemistry Letters*, 2019, **10**, 7629–7635.
38 L. Bonnet and J. Espinosa-García, *J.Chem. Phys.*, 2010, **133**, 164108.
39 C. Díaz, H. F. Busnengo, P. Rivière, D. Farías, P. Nieto, M. F. Somers, G. J. Kroes, A. Salin and F. Martín, *J. Chem. Phys.*, 2005, **122**, 154706.
40 C. C. Díaz, M. F. Somers, G.-J. Kroes, H. F. Busnengo, A. Salin and F. Martin, *Phys. Rev. B*, 2005, **72**, 035401.
41 D. Farias, C. Diaz, P. Nieto, A. Salin and F. Martin, *Chem. Phys. Lett.*, 2004, **390**, 250.
42 G.-J. Kroes and C. Díaz, *Chem. Soc. Rev.*, 2016, **45**, 3658.
43 C. Resh, H. F. Berger and K. D. Rendulic, *Surf. Sci.*, 1994, **L1105**, 316.
44 C. Resh, H. F. Berger and K. D. Rendulic, *Chem. Phys. Lett.*, 1995, **247**, 249.
45 W. H. Miller, *J. Chem. Phys.*, 1970, **53**, 3578–3587.
46 G. Campolieti and P. Brumer, *J. Chem. Phys.*, 1992, **96**, 5969–5982.
47 L. Bonnet, *J. Chem. Phys.*, 2018, **148**, 194104.
48 H. Kreek and R. A. Marcus, *J. Chem. Phys.*, 1974, **61**, 3308–3312.
49 C. W. McCurdy and W. H. Miller, *J. Chem. Phys.*, 1977, **67**, 463–468.
50 Y. Elran and K. G. Kay, *J. Chem. Phys.*, 2001, **114**, 4362–4376.
51 D. J. Tannor and S. Garashchuk, *Annu. Rev. Phys. Chem.*, 2000, **51**, 553–600.
52 Y. Elran and K. G. Kay, *J. Chem. Phys.*, 2002, **116**, 10577–10588.
53 M. Micciarelli, R. Conte, J. Suarez and M. Ceotto, *J. Chem. Phys.*, 2018, **149**, 064115.
54 M. Buchholz, F. Grossmann and M. Ceotto, *J. Chem. Phys.*, 2018, **148**, 114107.
55 M. C. Gutzwiller, *Chaos in Classical and Quantum Mechanics*, Springer-Verlag, New York, 1990.
56 L. Bonnet and C. Crespos, *Phys. Rev. A*, 2008, **78**, 062713.
57 L. Bonnet and J. C. Rayez, *Chem. Phys. Lett.*, 2004, **397**, 106–109.
58 L. Bonnet, *Chin. J. Chem. Phys.*, 2009, **22**, 210–214.
59 L. Bonnet, *Int. Rev. Phys. Chem.*, 2013, **32**, 171–228.
60 H. F. Busnengo, C. Crespos, W. Dong, J. C. Rayez and A. Salin, *J.Chem. Phys.*, 2002, **116**, 9005.
61 W. Dong and J. Hafner, *Phys. Rev. B*, 1997, **56**, 15396.
62 H. F. Busnengo, E. Pijper, G. J. Kroes and A. Salin, *The Journal of Chemical Physics*, 2003, **119**, 12553–12562.
63 H. Busnengo, E. Pijper, M. Somers, G. Kroes, A. Salin, R. Olsen, D. Lemoine and W. Dong, *Chem. Phys. Lett.*, 2002, **356**, 515.